PHYSICAL REVIEW B **91**, 035429 (2015)

# Scattering of phonons by high-concentration isotopic impurities in ultrathin graphite

Michael Thompson Pettes,[1,3] Mir Mohammad Sadeghi,[1] Hengxing Ji,[1,4] Insun Jo,[2] Wei Wu,[3] Rodney S. Ruoff,[1] and Li Shi[1,*]
[1]*Department of Mechanical Engineering, Texas Materials Institute, The University of Texas at Austin, Austin, Texas 78712, USA*
[2]*Department of Physics, The University of Texas at Austin, Austin, Texas 78712, USA*
[3]*Department of Mechanical Engineering, Institute of Materials Science, University of Connecticut, Storrs, Connecticut 06269, USA*
[4]*Department of Materials Science and Engineering, CAS Key Laboratory of Materials for Energy Conversion, University of Science and Technology of China, Hefei 230036, China*

(Received 21 January 2014; revised manuscript received 29 November 2014; published 21 January 2015)

As the isotopic concentration of ultrathin graphite is varied from natural abundance to nearly pure $^{13}$C, the thermal conductivity displays a slight dependence on the isotope concentration at temperatures near its maximum ~150 K. The strength of phonon-isotope scattering in the high-isotope impurity-concentration regime is found to be well below that given by a commonly used incoherent and independent isotope impurity scattering model. This finding is in agreement with some recent theoretical predictions that coherent multiple scattering of phonons is important in the measured thermal conductivity of low-dimensional materials in the high-isotope impurity-concentration regime.

DOI: 10.1103/PhysRevB.91.035429 PACS number(s): 65.80.Ck, 63.20.kp, 63.22.−m, 68.65.−k

## I. INTRODUCTION

Phonon scattering by isotopic impurities is an important mechanism for manipulating the thermal conductivity $\kappa$ of high-$\kappa$ materials that are actively investigated for thermal management applications [1,2]. Experiments on three-dimensional (3D) cubic crystals including diamond, silicon, and germanium [3–5] have shown that isotopic impurities considerably suppress the thermal conductivity at intermediate temperatures near the peak in $\kappa$. Two-dimensional (2D) hexagonal layered structures, such as single-layer graphene [6] and hexagonal boron nitride (*h*-BN) [7,8], as well as quasi-2D bulk graphite [9,10] and *h*-BN [11], are known to possess high in-plane $\kappa$ due to large crystallite sizes, light atomic masses, and strong interatomic bonding in the basal plane. Isotope impurity scattering in the low-concentration independent scattering regime [12] is relatively well understood for both 3D [13] and 2D [14,15] cases, although there is still uncertainty in the exact scattering rate expression for quasi-2D graphite. In comparison, a number of coherent scattering phenomena have been predicted for isotope impurity scattering in the high-concentration regime [14,16,17] and remain to be better understood. In this regime, whether and how interference among the scattered lattice waves can play an important role in the measured thermal conductivity is one of the central topics in recent phonon transport investigations [16]. One issue in question is whether such wave interference can result in an observable phonon localization phenomenon and a much stronger isotope-scattering effect than that predicted by the incoherent independent scattering theories [16]. In comparison, interference of scattered electromagnetic waves by particle agglomerates in the dependent multiple-scattering regime has been shown to result in a smaller scattering cross section than that predicted by the independent scattering theory [18–20]. Although it has also been predicted that multiple scattering of phonons in one-dimensional nanotubes [16] can result in weaker phonon-isotope scattering than that calculated with such a wave interference effect ignored, it is unclear whether such an effect is important in existing measured thermal conductivity results of nanotubes [21], graphene [22], diamond [3], and germanium [4] with high-isotope impurity concentrations. Clarifying this question is essential not only for correctly evaluating the impact of phonon isotope scattering on thermal conductivity, but also for developing the currently lacking knowledge in coherent phonon transport phenomena, the study of which has recently been limited mainly to thin-film superlattice structures [23,24].

Here we report a study of the effects of isotope impurity scattering on the measured thermal conductivity of high-quality ultrathin graphite (UG) samples with both low- and high-isotope impurity concentrations. The peak thermal conductivity of the UG samples occurs at a temperature close to 150 K and is reduced in a UG sample with about 50-at.% $^{13}$C and 50-at.% $^{12}$C compared to two other UG samples with 1.1- and 99.2-at.% $^{13}$C, respectively. However, our analysis suggests that the reduction is well below those predicted by an independent incoherent isotope-scattering model derived from perturbation theory, although the phonon dispersion of the isotopically disordered graphite can still be obtained from the virtual crystal approximation with the use of an average mass. Such a discrepancy is in agreement with recent theoretical predictions of the effects of multiple scattering of phonons by high-concentration isotope impurities in low-dimensional systems.

## II. EXPERIMENTAL METHODS AND RESULTS

The UG was synthesized with chemical vapor deposition (CVD) on the surface of commercially available nickel foams as discussed in Ref. [25]. The isotopic concentration of each obtained ultrathin graphite foam (UGF) was controlled through the methane source: (i) 1.1-at.% $^{13}$C UGF used methane with the naturally occurring isotopic concentration (98.9-at.% $^{12}$C), (ii) 50.2-at.% $^{13}$C UGF used equal partial pressures of natural methane and isotopically enriched $^{13}$C methane (99.2-at.% $^{13}$C), and (iii) 99.2-at.% $^{13}$C UGF used isotopically enriched $^{13}$C methane. The nickel was etched

---

[*] Corresponding author: lishi@mail.utexas.edu

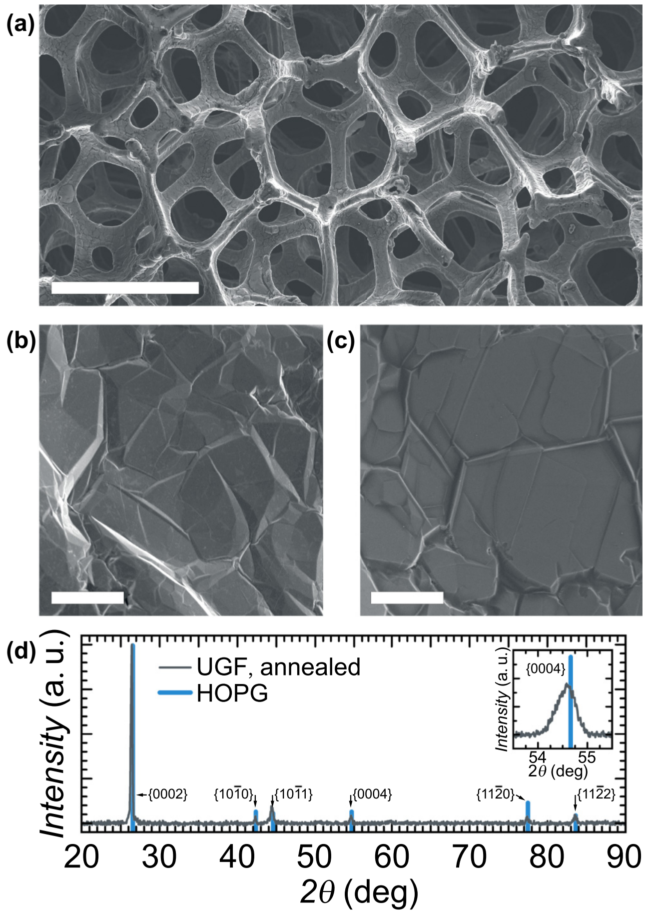

FIG. 1. (Color online) SEM images of (a) UGF, (b) the surface of as-grown UGF, and (c) the surface of UGF after postsynthesis annealing at 3000 °C. (d) XRD of the annealed UGF shown in comparison with the reflection positions of highly oriented pyrolytic graphite (HOPG) [56]. The intensities have been normalized to the {0002} peak. [(d), inset] High-resolution XRD of the {0004} peak.

using $(NH_4)_2S_2O_8$ (1 M) at 80 °C for about 1 week followed by $HNO_3$ (0.5 M) at 80 °C for about 3 days. In order to clearly observe the isotopic effect on thermal conductivity, the sample should possess high crystalline quality so as to minimize phonon scattering by defects and grain boundaries. We therefore performed postsynthesis annealing of the UGF at 3000 °C for 1 h in argon at positive pressure. A high-resolution scanning electron microscope (SEM) was used to examine the condition of the UGF strut walls before and after annealing. X-ray diffraction (XRD) was conducted using the Cu $K\alpha_1$ x-ray line, $\lambda = 0.154\,08$ nm. The unit-cell parameters were measured to be $a = b = 2.467\,5$ and $c = 6.745\,2$ Å before annealing and $a = b = 2.465\,9$ and $c = 6.737\,0$ Å after annealing. Based on SEM (Fig. 1) analysis, annealing the UGF had an observable effect on the surface morphology of the UG constituents, suggesting mesoscale ordering improvement in the highly ordered as-grown material was achieved upon annealing.

A high-precision electronic balance was used to determine the mass density and volume fraction of the UGF. The mass densities of the UGF samples were $(2.74 \pm 0.01) \times 10^{-2}$, $(2.40 \pm 0.01) \times 10^{-2}$, and $(2.67 \pm 0.01) \times 10^{-2}$ g cm$^{-3}$ for 1.1%, 50.2%, and 99.2% $^{13}$C, respectively. Based on the measured mass density data, the corresponding volume fractions $\varphi$ of the UGF in this paper are 1.21 ± 0.05, 1.06 ± 0.05, and 1.19 ± 0.06 vol. % for the samples with 1.1%, 50.2%, and 99.2% $^{13}$C, respectively. The $\varphi$ values are comparable to those reported in other recent papers [25,26]. Based on the measured volume fraction and pore size, the wall thickness of the synthesized UG is estimated in the range between tens of nanometers and nearly micrometer scale.

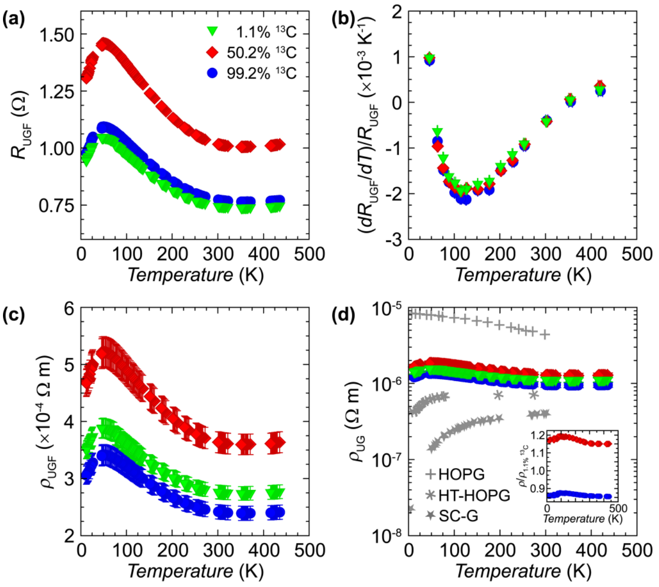

FIG. 2. (Color online) Temperature-dependent electrical properties of UGF after postsynthesis annealing. The isotopic concentration of $^{13}$C in $^{12}$C for the UGF samples is 1.1% (green down triangles), 50.2% (red diamonds), and 99.2% (blue circles). (a) Measured low-bias electrical resistance ($R_{UGF}$) and (b) normalized low-bias resistance change with temperature at each temperature $(dR_{UGF}/dT)/R_{UGF}$. (c) Electrical resistivity ($\rho_{UGF}$) of the UGF. (d) Solid electrical resistivity of the ultrathin graphite ($\rho_{UG}$) within the UGF, calculated using the foam theory of Lemlich [27], $\rho_{UG} = (\phi/3)\rho_{UGF}$, where $\varphi$ is the volume fraction. Shown in comparison are values for highly oriented pyrolytic graphite deposited at 2250 °C (HOPG, gray crosses) [57], HOPG deposited at 2200 °C, subsequently heat-treated HOPG (HT-HOPG) at 3200 °C (gray asterisks) [10], and single-crystal graphite (SC-G, gray stars) [58]. [(d), inset] $\rho_{UG}$ of the 50.2- and 99.2-at. % $^{13}$C samples normalized by that of the 1.1-at. % $^{13}$C sample. The legend shown in panel (a) applies to panels (a)–(d).

Compared to planar few-layer graphene or UG grown by CVD on a planar nickel substrate with a comparable layer thickness, the macroscopic size of the UGF structure used in this study allows it to be handled and measured relatively readily by an electrothermal method over a large temperature range [25] (see Appendix A). The measured electrical resistance of the UGF $R_{UGF}$ is shown in Fig. 2 along with the electrical resistivities of the UGF $\rho_{UGF}$, the UG within the UGF $\rho_{UG}$, and the normalized change in electrical resistance with the temperature of the UGF. The solid electrical resistivity of the UG strut walls was calculated using the foam theory of Lemlich [27], $\rho_{UG} = (\phi/3)\rho_{UGF}$. We note that the room temperature $\rho_{UG}$ of the 50.2- and 99.2-at. % $^{13}$C

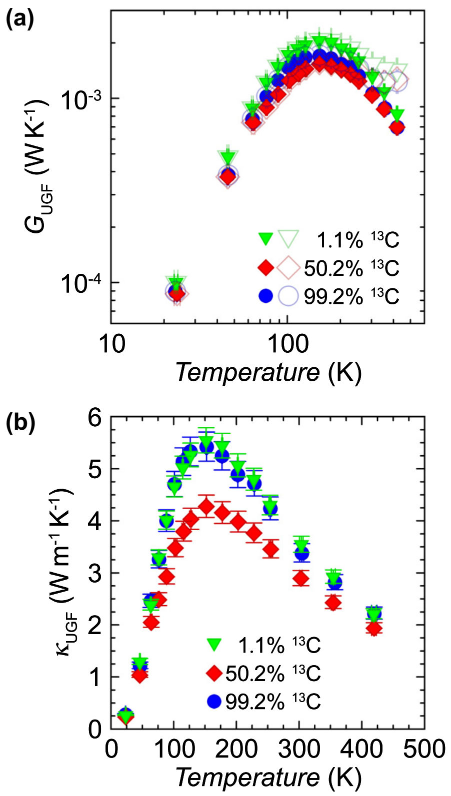

FIG. 3. (Color online) (a) Measured thermal conductance of the UGF samples ($G_{\mathrm{UGF}}$) determined with (filled symbols) and without (open symbols) the inclusion of radiation in the heat transfer model, i.e., Eqs. (3) and (5) in Ref. [25], respectively. The isotopic concentration of $^{13}$C in $^{12}$C for the UGF samples is 1.1% (green down triangles), 50.2% (red diamonds), and 99.2% (blue circles). (b) Measured effective thermal conductivity of the UGF ($\kappa_{\mathrm{UGF}}$) versus temperature. The legend shown in panel (a) applies to panels (a) and (b).

samples is approximately 15% higher and 14% lower than that of the 1.1-at. % $^{13}$C sample. Such small variation in the electrical resistivity can be caused by similar variations in the charge-carrier concentration or mobility in the three samples.

The effective thermal conductance of the UGF $G_{\mathrm{UGF}}$ is shown in Fig. 3 and was obtained from the electrical resistance $R_{\mathrm{UGF}}$, measured during electrical self-heating of the UGF by coupling a small ac current ($\sim 10^{-3}$ A) to the dc current and measuring the ac voltage drop using a lock-in amplifier. When the frequency of the ac current is sufficiently high compared to the thermal response of the sample [25,28], the average temperature rise in the suspended UGF $\bar{\theta}$ can be obtained from the $R_{\mathrm{UGF}}$ measured by the lock-in technique and the measured $dR_{\mathrm{UGF}}/dT$. $G_{\mathrm{UGF}}$ can then be obtained using the following expression incorporating radiation heat loss from the sample surface [25,29]:

$$G_{\mathrm{UGF}} \equiv \frac{\kappa_{\mathrm{UGF}} A}{L} = -\frac{\dot{Q}}{m^2 L^2 \bar{\theta}}\left[\frac{2}{mL}\tanh(mL/2) - 1\right], \quad (1a)$$

where

$$m \equiv \sqrt{\frac{h_r P}{\kappa_{\mathrm{UGF}} A}}, \quad (1b)$$

and

$$h_r = 4\varepsilon_{\mathrm{UGF}}(T_0)\,\sigma\,T_0^3. \quad (1c)$$

In the above equations, $L$ is the suspended length of the sample, $P = 2(w + t)$ and $A = wt$ are the effective perimeter and cross-sectional area, respectively, $w$ and $t$ are the width and thickness, respectively, $\varepsilon_{\mathrm{UGF}}(T)$ is the temperature-dependent total hemispherical emissivity and was measured to be near unity [25], $\sigma$ is the Stefan-Boltzmann constant, and $T_0$ is the environment temperature. The measured thermal conductance data of the UGF samples suggest that the radiation loss is not negligible at high temperatures and if not accounted for can lead to overestimation of $G_{\mathrm{UGF}}$ by 17%–21% at room temperature but only contributes less than 5% to the total thermal conductance below 200 K. With the radiation heat loss accounted for, the effective thermal conductivity of the UGF $\kappa_{\mathrm{UGF}}$ reached a maximum of $5.5 \pm 0.2$, $4.3 \pm 0.2$, and $5.4 \pm 0.3$ W m$^{-1}$ K$^{-1}$ for 1.1%, 50.2%, and 99.2% $^{13}$C isotopic concentrations at $\sim$150 K, respectively (Fig. 3).

To determine the solid thermal conductivity $\kappa_{\mathrm{UG}}$ of the UG within the UGF, we use the approach of Schuetz and Glicksman [30] to obtain $\kappa_{\mathrm{UG}} = (3/\Phi)\kappa_{\mathrm{UGF}}$, which is shown in Fig. 4. The $\kappa_{\mathrm{UG}}$ of the UGF samples reached a maximum of $1375 \pm 85$, $1209 \pm 86$, and $1369 \pm 101$ W m$^{-1}$ K$^{-1}$ for 1.1%, 50.2%, and 99.2% $^{13}$C isotopic concentrations at $\sim$150 K, respectively, illustrating a small effect of isotopic impurity scattering at temperatures near the peak in thermal conductivity. We note that the uncertainty expressed in the above solid thermal conductivity values is mainly due to the uncertainty in measured density and hence volume fraction, which is on the order of 4% to 5% and does not affect the observed temperature-dependent trends. The variation in room temperature $\kappa_{\mathrm{UG}}$ was marginal and comparable to the measurement uncertainty $880 \pm 54$, $819 \pm 58$, and $854 \pm 63$ W m$^{-1}$ K$^{-1}$ for 1.1%, 50.2%, and 99.2% $^{13}$C isotopic concentrations, respectively. Above room temperature, $\kappa_{\mathrm{UG}}$ is found to decrease rapidly with increasing temperature, suggesting phonon-phonon scattering processes are dominant at this temperature range in the highly ordered crystalline materials. In addition, the solid thermal conductivity values for the three samples are nearly identical at temperatures below about 50 K, suggesting that the grain sizes are similar for the three samples because grain-boundary scattering is expected to be the dominant mechanism in the low-temperature regime.

In order to gain a better understanding of the phonon dynamics underlying the observed thermal conductivity results, the UGF samples were characterized with Raman spectroscopy at different laser excitation energies of 1.96 eV (632.8 nm), 2.41 eV (514.5 nm), and 2.54 eV (488.0 nm). The Raman measurements were carried out after calibration to the first-order peak associated with scattering by the zone-center optical-phonon polarization of crystalline Si (111) at $\sim$520 cm$^{-1}$ [31,32]. As shown in Fig. 5, other than the $G$ peak associated with scattering by the longitudinal-optical (LO) polarization at the Brillouin-zone center [33], no other first-order peaks (e.g., $D$ peak) were detected for the UGF. As the $D$ peak is associated with scattering between excited electrons and one in-plane transverse-optical (iTO) phonon and one defect, the absence of the $D$ peak in the Raman spectra reveals the high crystal quality of the CVD UGF samples. The measured

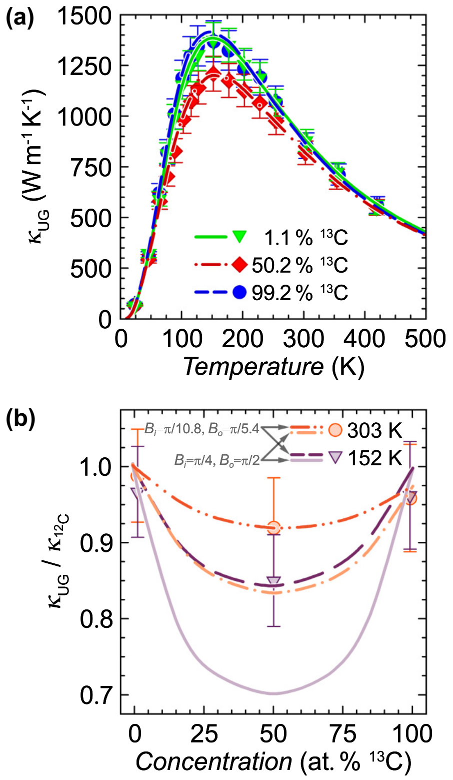

FIG. 4. (Color online) (a) Solid thermal conductivity of the UG ($\kappa_{\mathrm{UG}}$) versus temperature for $^{13}$C concentration of 1.1% (green down triangles), 50.2% (red diamonds), and 99.2% (blue circles). The lines are the calculated thermal conductivity based on the fitting parameters discussed in the text for different $^{13}$C concentrations. (b) Calculated solid thermal conductivity normalized by the theoretical value for isotopically pure $^{12}$C graphite ($\kappa_{\mathrm{UG}}/\kappa_{^{12}\mathrm{C}}$) as a function of $^{13}$C isotopic concentration at temperatures of 152 K (purple down triangles) and 303 K (orange circles). In one calculation, the isotope-scattering coefficient $B$ is taken to be $B_i = \pi/4$ for the in-plane mode and $B_o = \pi/2$ for the out-of-plane modes. In another calculation, the two $B$ coefficients are reduced to $B_i = \pi/10.8$ for the in-plane mode and $B_o = \pi/5.4$.

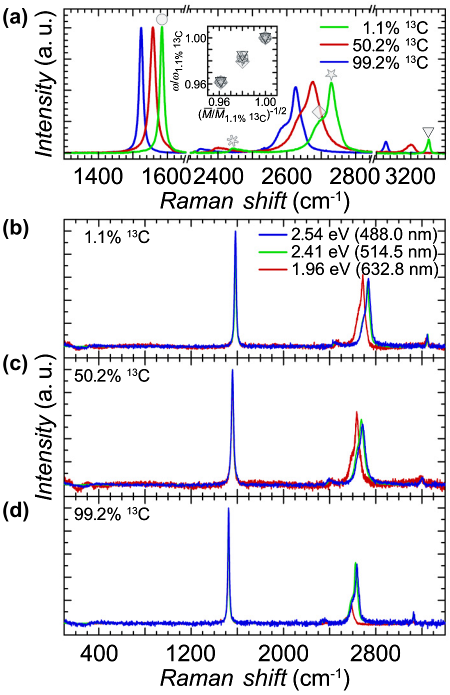

FIG. 5. (Color online) (a) Raman spectra normalized to the *G* peak intensity using 2.41-eV laser energy. The isotopic concentration of $^{13}$C in $^{12}$C for the UGF samples is 1.1% (green line), 50.2% (red line), and 99.2% (blue line). [(a), inset] The Raman peak positions ($\omega$) normalized by those for 1.1-at. % $^{13}$C UGF exhibit the predicted dependence on the average atomic mass for Raman-active phonon modes, i.e., $\omega/\omega_{1.1\%\ ^{13}\mathrm{C}} = (\overline{M}/\overline{M}_{1.1\%\ ^{13}\mathrm{C}})^{-1/2}$. The Raman peaks are labeled on the 1.1-at. % $^{13}$C spectra in the main panel where circles and down triangles correspond to near-zone-center LO and 2LO processes, respectively, and asterisks, diamonds, and stars denote near-zone-boundary iTO + LA, 2iTO along Γ–K, and 2iTO along K–M processes, respectively. (b)–(d) Raman spectra of graphite foams with (b) 1.1%, (c) 50.2%, and 99.2% $^{13}$C excited by 2.54-eV (blue), 2.4-eV (green), and 1.96-eV (red) laser energies. Legend in (b) applies to all panels (b)–(d).

Raman spectra contain second-order peaks associated with double-resonance scattering by two LO phonons near the zone center, by two iTO phonons near the zone boundary, and by one iTO phonon and one longitudinal-acoustic (LA) phonon near the zone boundary [33–35]. Whereas the first-order peaks are insensitive to excitation energy, these second-order peaks exhibit apparent dependence on the laser excitation energy as shown in Fig. 5. Such dependence can be used to extract the phonon dispersion of the UGF samples with different isotope impurity concentrations as discussed below and in Appendix C.

## III. THEORETICAL ANALYSIS

One critical question is on the effect of isotopic disorder on the phonon dispersion of the UGF samples. In particular, it is important to evaluate whether the phonon dispersion of the high-isotope impurity-concentration sample can still be described with the virtual crystal approximation [36] where the system is approximated as a homogeneous crystal with a single average mass ($\overline{M}$) of the actual crystal with isotope impurities. To address this question, we have first calculated the phonon dispersions for each isotopic concentration at which $\kappa_{\mathrm{UG}}$ is calculated, from pure $^{12}$C to pure $^{13}$C, using the virtual crystal approximation and *ab initio* density functional perturbation theory (QUANTUM ESPRESSO) [37]. In accordance with a prior paper [38], the phonon-dispersion calculations were based on fixed lattice constants of $a = 2.458$ and $c = 6.701$ Å, the generalized gradient approximation, and a plane-wave basis set with a wave-function cutoff of 60 Ry and a charge-density cutoff of 600 Ry with ultrasoft pseudopotentials for carbon created by the Rappe-Rabe-Kaxiras-Joannopoulos (RRKJ) method. The plane-wave self-consistent calculations were carried out on a $k$-point grid of $8 \times 8 \times 4$. The interatomic force constants were calculated from dynamic matrices on a $5 \times 5 \times 4$ Monkhorst-Pack $q$-vector phonon grid that allowed for determination of the phonon frequencies at arbitrary wave vectors $q$. As shown in Fig. 6, the obtained zone-boundary optical-phonon frequency and sound velocities exhibit the

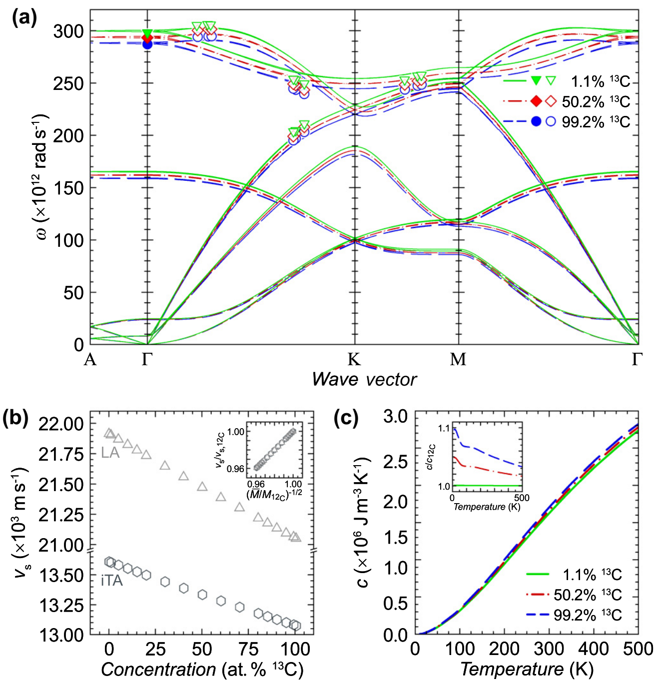

FIG. 6. (Color online) (a) Calculated phonon dispersion for bulk graphite with 1.1-at. % $^{13}$C (green solid lines), 50.2-at. % $^{13}$C (red dashed-dotted lines), and 99.2-at. % $^{13}$C (blue dashed lines) isotopic concentrations using the virtual crystal approximation. Experimental dispersion data obtained from first-order (filled symbols) and derived from second-order (open symbols) Raman scattering using an *ab initio* electron band-structure calculation for graphite is shown for UGF with $^{13}$C concentrations of 1.1% (green down triangles), 50.2% (red diamonds), and 99.2% (blue circles). (b) Near-zone-center phonon group velocity (sound velocity, $v_s \equiv \lim_{\mathbf{q}\to 0} \nabla_{\mathbf{q}}\omega$) taken along Γ-M for the LA and in-plane transverse acoustic (iTA) polarizations as a function of $^{13}$C isotopic concentration. [(b), inset] The sound velocities normalized by that for $^{12}$C graphite exhibit the expected dependence on atomic mass, i.e., $v_s/v_{s,\,^{12}\mathrm{C}} = (\overline{M}/M_{^{12}\mathrm{C}})^{-1/2}$. (c) Calculated volumetric specific heat $c$ versus temperature for $^{13}$C concentrations of 1.1 at. % (green solid line), 50.2 at. % (red dash-dot line), and 99.2 at. % (blue dashed line). [(c), inset] Due to the reduced group velocity of isotopically enriched graphite, $c$ for 50.2- and 99.2-at. % $^{13}$C is higher than that for pure $^{12}$C at the temperature range of calculation, i.e., below 500 K.

expected $\overline{M}^{-1/2}$ dependence. In addition, it is worth noting that the specific heat calculated from the obtained dispersion for 50.2- and 99.2-at. % $^{13}$C is higher than that for pure $^{12}$C at low temperatures due to the reduced group velocity of the isotopically enriched material.

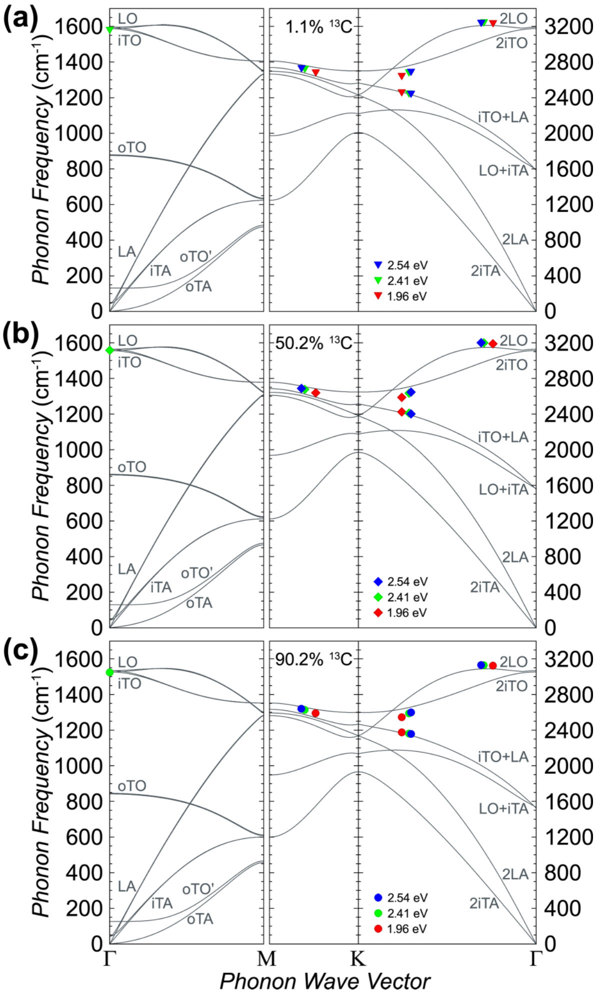

FIG. 7. (Color online) First-order (left panel) and second-order (right panel) Raman modes measured in the UGF samples with (a) 1.1%, (b) 50.2%, and (c) 90.2% $^{13}$C in comparison with *ab initio* phonon dispersions. Red, green, and blue symbols indicate experimental data obtained using laser exitations at 1.96 eV (632.8 nm), 2.41 eV (514.5 nm), and 2.54 eV (488.0 nm), respectively.

In order to evaluate the accuracy of the phonon dispersion calculated with the virtual crystal approximation, the first- and second-order Raman peak positions obtained at different laser energies were analyzed according to an approach similar to those reported recently [33–35] to obtain the phonon energies at different phonon wave vectors. Instead of making the isotropic linear dispersion assumption at the K and K′ points, we obtained the excited and scattered electron wave vectors using an *ab initio* electron band structure for graphite calculated by density functional theory [37] in a method similar to Ref. [38] (see Appendix B). In addition, the electron energy loss by phonon scattering is accounted for in our analysis as explained in Appendix C. As shown in Fig. 7, the mapping of the measured 2LO, 2iTO, and iTO + LA Raman modes along the Γ–K direction and the first-order mode all match well with the *ab initio* phonon dispersion calculated with the virtual crystal approximation. The mapping of the measured 2iTO frequency along K–M is just somewhat lower than the *ab initio* phonon dispersion.

We note that the virtual crystal approximation does not take into account the exact atomic positions of atomic impurities. However, the mass difference between $^{12}$C and $^{13}$C is small so that the calculated phonon dispersions for nearly pure $^{12}$C and $^{13}$C graphite are still rather similar. In addition, our measured Raman $G$ peak and 2$D$ peaks even for the 50% $^{13}$C graphite sample are still rather similar to those of low-isotopic impurity concentrations. Moreover, the measured Raman peak positions for both near-zone-center and near-zone-boundary phonons clearly exhibit the $\overline{M}^{-1/2}$ dependence predicted by the virtual crystal approximation [Fig. 5(a), inset], in agreement with earlier measurements of graphene with different isotope concentrations [22,39]. Hence, even the 50% impurity concentration sample can still be treated as a virtual crystal with clearly defined phonon dispersion of graphite as opposed to a highly disordered system or amorphous solid. As such, the thermal conductivity of the isotopically disordered graphite samples should still be described by that established for crystals with well-defined lattice vibration modes, instead of with the Allen-Feldman diffusion model [40] for describing random walks of thermal energy in disordered or amorphous solids.

Hence, we have analyzed the measurement results with a theoretical model for in-plane bulk graphite thermal conductivity based on the following solution to the Boltzmann transport equation under the relaxation time approximation (RTA) [41] and with the use of the full phonon dispersion calculated for the entire Brillouin zone of graphite [42]:

$$\kappa_{\mathrm{UG}} = \sum_{p=1}^{6} \kappa_p = \frac{\hbar^2}{8\pi^3 k_{\mathrm{B}} T^2} \sum_{p=1}^{6} \sum_{q=0}^{q_{max}} \tau_p v_{x,p}^2 \omega_p^2 \times \frac{e^{\hbar\omega_p/k_B T}}{\left(e^{\hbar\omega_p/k_B T} - 1\right)^2} \Delta q^3, \qquad (2)$$

where $\hbar$ and $k_{\mathrm{B}}$ are the reduced Planck constant and Boltzmann constant, respectively, $T$ is the temperature, $\tau$ is the relaxation time, $\omega$ and $q$ are the phonon angular frequency and wave vector, respectively, $\Delta q^3$ is the volume of each element within the discretized Brillouin zone, and $v_x$ is the component of phonon group velocity ($v$) parallel to the transport direction. The subscript $p$ denotes each of the six lowest-lying phonon polarizations of $AB$ stacked graphite. The direct contribution of the six remaining optical modes to the thermal conductivity is expected to be small due to low occupation probability in the temperature range considered here as well as strong scattering of high-frequency modes [15]. This model does not include the Callaway term for correcting normal scattering [4,5,43] because such a correction is found to be important only for highly pure low-defect samples and is deemed to be unnecessary for the polycrystalline samples with appreciable isotope impurity concentrations [4].

To calculate the total relaxation times $\tau$ for each phonon polarization, we consider the contributions of phonon-boundary ($\tau_b$), phonon-impurity ($\tau_i$), and anharmonic phonon-phonon ($\tau_{anh}$) scattering processes. These contributions are combined according to Matthiessen's rule $\tau^{-1} = \tau_b^{-1} + \tau_i^{-1} + \tau_{anh}^{-1}$. Phonon-boundary scattering for a given mean-free path for all polarizations $l_b$ is obtained as ${\tau_b}^{-1} = |v|/l_b$. In the incoherent independent scattering regime, phonon-isotope impurity scattering has been obtained according to a commonly used analytical model derived by Tamura [13], based on the original model of Klemens [12] and perturbation theory, and later refined by Lindsay *et al.* for graphene as [15]

$$\tau_i^{-1} = B g_2 V_0 \omega^2 D(\omega), \quad g_2 = \sum_j c_j \left(1 - M_j/\overline{M}\right)^2, \qquad (3)$$

where $g_2$ is the second-order mass variance parameter, $c_j$ is the $j$th impurity concentration, $M_j$ and $\overline{M}$ are the $j$th impurity and average atomic masses in a crystal with mixed isotopes, respectively, $V_0 = 3^{3/2} a_{\mathrm{c-c}}^2 \delta/4$ is the volume per atom, $a_{\mathrm{c-c}}$ and $\delta$ are the carbon-carbon nearest-neighbor distance and interlayer spacing, respectively, $D(\omega)$ is the polarization-specific phonon density of states, and $B$ is a polarization-independent constant. The value of $B$ has been derived as $\pi/6$ for a three-dimensional cubic crystal [13] and becomes $\pi/4$ and $\pi/2$ for the in-plane and flexural (out-of-plane) phonon polarizations of two-dimensional graphene [15].

Compared to the original model by Klemens [12], the models of Tamura [13] and Lindsay *et al.* [15] do not assume the Debye approximation and allowed for the use of the actual phonon dispersion and density of states, which are calculated from first principles and incorporated into the isotope-scattering model with a numerical approach in this paper. The validity of these different versions of the Klemens model in the high-isotope impurity-concentration regime is the focus of this paper and examined in a subsequent section.

The umklapp phonon-phonon scattering rate is calculated according to the relaxation time approximation of Klemens and Pedraza [44],

$$\tau_{anh}^{-1} = 2\gamma^2 \frac{k_{\mathrm{B}} T}{M_{\mathrm{unit\_cell}} v^2} \frac{\omega^2}{\omega_{\max}}, \qquad (4)$$

where $\gamma$ is the polarization-specific Grüneisen parameter, $M_{\mathrm{unit\_cell}}$ is the mass of the graphite unit cell, and $\omega_{\max}$ is the zone-boundary frequency for each phonon polarization [45]. The Grüneisen parameters in Eq. (4) are modeled as in Ref. [25] $\gamma = aT^n$, where $a$ and $n$ are polarization-specific adjustable parameters made in observance of the wave-vector dependence of $\gamma$ reported in Ref. [38]. The calculated Grüneisen parameters for the out-of-plane transverse polarizations [out-of-plane transverse-acoustic (oTA) and out-of-plane transverse-optical (oTO′) in Fig. 7] and high-frequency optical polarizations are much larger in magnitude than for the in-plane transverse and longitudinal modes [38]. Consequently, Eq. (4) results in strong phonon-phonon scattering of these polarizations, and the calculated $\kappa_{\mathrm{UG}}$ is dominated by the in-plane acoustic and low-lying optical (LA, iTA, LO′, and iTO′) polarizations in graphite.

By fitting the theoretical model with the low-temperature experimental $\kappa_{\mathrm{UG}}$, the phonon-boundary scattering mean-free path $l_b$ was found to be 3.83 $\mu$m for all samples. This value is 2.6 times larger than $l_b$ for the unannealed thick-layered samples reported in Ref. [25] and indicative of the beneficial effect of postsynthesis thermal treatment at 3000 °C. Grüneisen parameters of $\gamma_{\mathrm{LA}} = \gamma_{\mathrm{LO'}} = 0.136T^{0.568}$ and $\gamma_{\mathrm{iTA}} = \gamma_{\mathrm{iTO'}} = 0.055T^{0.568}$ were used to match the calculation results with the high-temperature thermal conductivity values for all samples. As shown in Fig. 4, although the calculated $\kappa_{\mathrm{UG}}$ values based on $B = \pi/4$ for the in-plane polarized modes fit well over the entire temperature range for the low-impurity-concentration regimes, this $B$ value considerably overpredicts the strength of isotope scattering in the 50% $^{13}$C sample compared to the experimental results. The isotope-scattering strength needs to be reduced by nearly a factor of 2.75 by using $B = \pi/11$ for the in-plane polarized modes in order to match the calculation result to the measured $\kappa_{\mathrm{UG}}$ of the 50% $^{13}$C sample. At this reduced $B$ value, the largest thermal conductivity reduction for isotopic impurity scattering with respect to pure $^{12}$C, about 19%, occurs for 50% $^{13}$C at a temperature of ~125 K. For other temperatures, the maximum reduction in $\kappa$ in comparison with isotopically pure $^{12}$C is about 18%, 14%, 8%, and 6% at 100, 200, 300, and 400 K, respectively.

In the above calculation, the RTA expressions of Klemens and Pedraza [44] yield a negligible thermal conductivity contribution from the oTA branch. However, the oTA polarization dominates the specific heat at low temperatures. A recent first-principles calculation by Lindsay *et al.* has suggested that the thermal conductivity contribution from the oTA branch in graphite is not as important as that in suspended graphene but is not negligible [15]. Hence, in addition to the above calculation for the limit of negligible oTA contribution to the thermal conductivity, we have adjusted the Grüneisen parameters for each polarization to obtain another limit where the relative contribution from the oTA polarization in graphite is as large as that calculated by Lindsay *et al.* for five-layer graphene. In this case, although the independent isotope-scattering model can fit the measured thermal conductivity of the two low-isotope concentration samples, the isotope-scattering rate needs to be reduced by a factor of 12.5 from the independent scattering model in order to fit the sample with 50% $^{12}$C and 50% $^{13}$C as shown in Appendix D.

Hence, the two calculations for both negligible and significant oTA contributions suggest that the isotope-scattering rate in the high-concentration sample is considerably smaller than that calculated by the independent scattering model. This discrepancy can be either caused by the inaccuracy in the calculation of the phonon-defect or phonon-phonon scattering, or suggest the failure of the independent isotope-scattering model in the high-isotope concentration regime. For example, the isotope effect is expected be small in samples with a high concentration of other point defects, such as vacancies besides isotope impurity. However, such point defects are expected to yield an observable Raman *D* peak, which is absent for our samples. Another possibility is that the ignorance of the correction term for the normal processes in the two calculations results in an underestimation of the thermal conductivity contribution from the low-frequency long-wavelength phonons, which are not scattered much by isotope impurities. However, increasing the relative contribution from these low-frequency phonons is expected to alter the temperature dependence of the calculated thermal conductivity.

Although it remains a question whether the discrepancy is caused by the inaccuracy in the phonon-phonon scattering model used in the calculation, the discrepancy is in agreement with a recent theoretical finding of the lower-isotope-scattering rate in the high-concentration regime [16] than the independent scattering model [13]. In arriving at the independent scattering expression of Eq. (3) [13], Tamura assumed randomly distributed isotope impurities and dropped the phase factor and higher-order variance parameter terms $g_n \equiv \sum_j c_j(1 - M_j/\overline{M})^n$, in agreement with Klemen's assumption that interference terms cancel in the average for randomly distributed defects [46]. Even at these high-isotope concentrations, the difference between the atomic mass of any isotope from the average mass is still small so that $g_n$'s decrease rapidly with increasing $n$ above 2. Tamura considered corrections due to higher-order contributions to account for effects of wave interference due to multiple scattering by the same or different isotope sites [13] and concluded that such a correction was negligibly small for the case of a Ge sample with $g_2$, $g_3$, and $g_4$ being $5.87 \times 10^{-4}$, $7.1 \times 10^{-7}$, and $7.57 \times 10^{-7}$, respectively. Therefore, it has been assumed in most prior reports that such independent scattering expressions are still adequate in describing the experimental thermal conductivity data of 3D crystal structures in the high-isotope impurity regime. For example, such independent scattering models have been used for calculating the isotope impurity scattering rate in the high-isotope impurity regime for Ge, BN, and SiC [4,5] with $g_2$ values of $1.53 \times 10^{-3}$, $1.61 \times 10^{-3}$, and $1.45 \times 10^{-3}$, respectively. As one exception, Berman *et al.* [47] noted that their measured thermal conductivity results of LiF crystals at high-isotope concentrations were higher than those predicted by Klemens's independent scattering model, although they stated that the validity of the independent scattering expression is not limited explicitly to a particular range of concentrations, provided that the imperfections scatter only through their mass deviation. However, in a subsequent paper, Berman and Brock [48] stated that Klemens's isotope-scattering rate model could explain their LiF data even in the high-isotope impurity-concentration regime.

In comparison, $g_1 = g_3 = 0$, $g_2 = 1.6 \times 10^{-3}$, and $g_4 = 2.56 \times 10^{-6}$ for the 50% $^{13}$C sample. The $g_2$ value is still comparable to those for the reported Ge, BN, and SiC samples [4,5]. In addition, the $g_4/g_2$ is as small as $1.6 \times 10^{-3}$, which would still result in negligible higher-order corrections based on Tamura's analysis [13]. However, with wave interference effects due to multiple scattering accounted for in a Green's function calculation of the phonon transmission function, Savić *et al.* obtained the isotope-scattering rate was lower than the incoherent approximation by a factor of 2 or larger in carbon nanotubes and boron nitride nanotubes with isotope impurity concentration larger than 10% [16]. Although such a first-principles calculation remains an unresolved computational challenge for the complex UG samples measured in this experiment, the factor of 2 or larger difference found by Savić *et al.* for nanotubes is rather close to the reduction in the $B_i$ parameter from $\pi/4$ to $\pi/11$ in order to match the above calculation with the experimental $\kappa_{\mathrm{UG}}$ values of the 50% $^{13}$C sample. This similarity suggests that multiple scattering is an important factor of the reduced $B$ parameter.

## IV. SUMMARY

The enhanced crystal quality of the annealed 2D UG structures has enabled the experimental finding of the suppressed isotope-scattering rate in the high-isotope concentration regime compared to the incoherent independent isotope-scattering model, which has been assumed in most prior investigations to be adequate for analyzing experimental thermal conductivity data for crystals with high-isotope impurity concentrations. This finding is in agreement with two recent theoretical predictions [16,17] that wave interference effects due to multiple scattering are important in the high-isotope impurity regime in low-dimensional high-$\kappa$ materials where isotope scattering is an important mechanism. Hence, while phonon coherence effects have recently been suggested to be observable in the measured thermal conductivity of some thin-film superlattice structures [23,24], the experimental results reported in this paper emphasize another phonon transport process where consideration of coherent phonon transport is necessary. Additionally, our Raman measurement results show that the virtual crystal approximation is still accurate for the calculation of the phonon distribution in graphite with large isotope impurity concentrations. These findings are expected to motivate further investigations of theoretical computational models to accurately evaluate the coherence isotope-scattering effects in ultrathin graphite and other materials.

## ACKNOWLEDGMENTS

The authors thank W. Shih at Allcomp, Inc. for post-synthesis annealing of the UGF samples, Dr. D. P. Sellan for machining the graphite crucible used during annealing, and D. R. Jares for machining the copper blocks used in the measurements. The work was primarily supported by the U. S. Department of Energy, Office of Basic Energy Sciences Physical Behavior of Materials Program Award No. DE-FG02–07ER46377 (M.T.P. and L.S.). Theoretical computation by M.M.S. was supported by National Science Foundation Award No. EEC-1160494. Synthesis by H.J. and R.S.R. was supported by the Advanced Research Projects Agency–Energy High Energy Advanced Thermal Storage program Award No. DE-AR0000178. Additional theoretical calculations by I.J. were supported by the Office of Naval Research Award No. N00014-10-1-0581. X-ray diffraction, Raman spectroscopy analysis, and modeling by W.W. and M.T.P. were supported by the University of Connecticut. The authors thank Professor David A. Broido for helpful discussions.

## APPENDIX A: THERMAL CONDUCTIVITY MEASUREMENT

UGF samples, approximately 33–38-mm long, 4.9–5.8-mm wide, and 1.58–1.62-mm thick, were fixed at each end to a copper heat sink using a high thermal conductivity electrically insulating epoxy. Four electrodes were attached to the two ends of the suspended sample using an electrically conducting silver epoxy as shown in Fig. 8. The suspended length of the UGF samples was 25.0–25.5 mm. The samples were then placed into a vacuum cryostat connected to a turbomolecular pumping system, which maintained a vacuum level of ~$10^{-6}$ Torr. The local environment temperature surrounding the UGF samples was actively controlled through a cryogenic temperature controller. A direct current power supply and high power resistors were used to source a dc current $I_{\mathrm{dc}}$ through the suspended UGF, raising its temperature through Joule heating $Q = I_{\mathrm{dc}}^2 R_{\mathrm{UGF}}$.

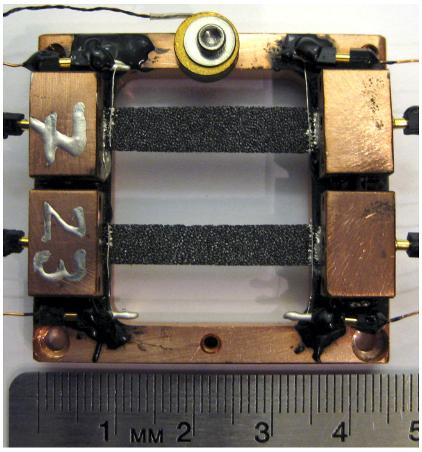

FIG. 8. (Color online) Top-view photograph of the experimental setup for measuring the electrical and thermal properties of UGF. Units of integers printed on ruler are in centimeters.

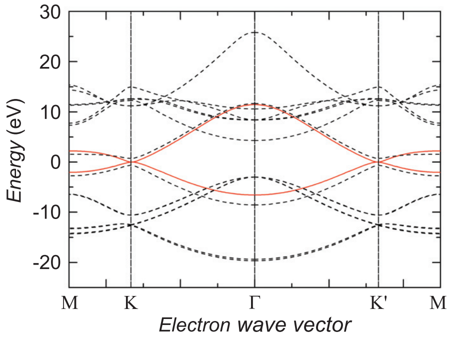

FIG. 9. (Color online) *ab initio* electron band structure of graphite. The red lines indicate the $\pi$ and $\pi^*$ bands, i.e., valence and conduction bands, respectively, along the Γ–K–M direction used in the electron-scattering analysis. Dashed lines indicate $\sigma$ and $\sigma^*$ bands.

## APPENDIX B: COMPUTATIONAL METHOD

The electron band structure of graphite was calculated using the *ab initio* calculation package QUANTUM ESPRESSO [37]. In accordance with Ref. [38], fixed lattice constants of $a = 2.458$ and $c = 6.701$ Å, the generalized gradient approximation, and a plane-wave basis set with a wave-function cutoff of 60 Ry and a charge-density cutoff of 600 Ry were used for all calculations with ultrasoft pseudopotentials for carbon created by the RRKJ method [49]. The plane-wave self-consistent calculations were carried out on a $k$-point grid of $8 \times 8 \times 4$. The electron band structure is shown along high-symmetry points in Fig. 9.

## APPENDIX C: RAMAN SPECTROSCOPY ANALYSIS

In order to obtain information about the phonon dispersion of isotopically disordered graphite, we have used Raman spectroscopy combined with an *ab initio* electron band-structure calculation. Quantitative analysis was conducted using multienergy Raman spectroscopy based on methods reported previously [33–35,50–53], which extract the phonon frequency-wave-vector relationship by varying the momentum of electron-hole pairs generated using multiple laser excitation energies.

Raman spectroscopy was conducted using a Ramascope System 2000 (Renishaw plc) with three different laser wavelengths after calibration to the first-order peak associated with scattering by the zone-center optical-phonon polarization of crystalline Si (111) at ~$520\,\mathrm{cm}^{-1}$ [31,32]. Laser excitation wavelengths of 488.0 nm (2.54 eV) and 514.5 nm (2.41 eV) were generated with an argon-ion source (Stellar-Pro Select 150, Modu-Laser, LLC), and the laser excitation wavelength of 632.8 nm (1.96 eV) was generated with a helium neon source (Research Electro-Optics, Inc.). The UG samples were supported on a glass substrate, and Raman spectra were collected for around 1 h each in order to increase the signal-to-noise ratio. The Raman *G* peak, corresponding to scattering with a single zone-center LO phonon, does not display excitation energy dependence, whereas the 2*D* peaks, corresponding to scattering by two phonons with nonzero wave vectors, display noticeable excitation energy dependence since the wave vector of the participating phonons is dependent on the wave vector of the excited electron-hole pair. This feature allows us to map the phonon frequency-wave-vector relationship of the isotopically engineered UG as discussed below.

#### 1. First-order Raman modes

Graphite's *G* peak arises from the $E_{2g}$ vibrational mode and is associated with the LO phonon polarization near the Γ point in the Brillouin zone so that the corresponding phonon wave vector of *G*-mode phonons is assigned at the Γ point [33]. Graphite's *D* peak is associated with scattering between excited electrons and one iTO phonon and one defect. In this study, no *D* mode was observed. This finding is indicative of the highly ordered nature of the CVD grown samples as evidenced by x-ray-diffraction analysis.

#### 2. Second-order Raman modes

The second-order process associated with an excited electron scattered by two phonons, instead of one phonon and one defect, comes from the double-resonant Raman-scattering processes shown in Fig. 10. The incident laser energy $E_1$ stimulates an electron from the valence band to the conduction band creating an electron-hole pair with a certain wave vector $k_1$. The excited electron's wave vector $k_1$ was determined by finding the electron-hole pair with energy difference $E_1$ around the K or K′ points of the *ab initio* electronic $\pi$ and $\pi^*$ bands depicted schematically in Figs. 10(b)–10(d). The excited electron is then inelastically scattered to another real state $E_2$ in which process a phonon is created. The real state $E_2$ with electron wave vector $k_2$ was obtained by the following expression:

$$E_2 = E_1 - \hbar\omega_{\mathrm{ph}}, \tag{C1}$$

where $\omega_{\mathrm{ph}}$ is the frequency of the created phonon. The electron at state $E_2$ is then inelastically scattered by a second phonon back to a virtual state which has the same electron wave vector as the real state $E_1(k_1)$. To calculate the phonon energy for the double-resonance processes, we must have information about which specific processes are involved. For example, the Raman 2*D* and 2*G* peaks involve scattering by two identical iTO

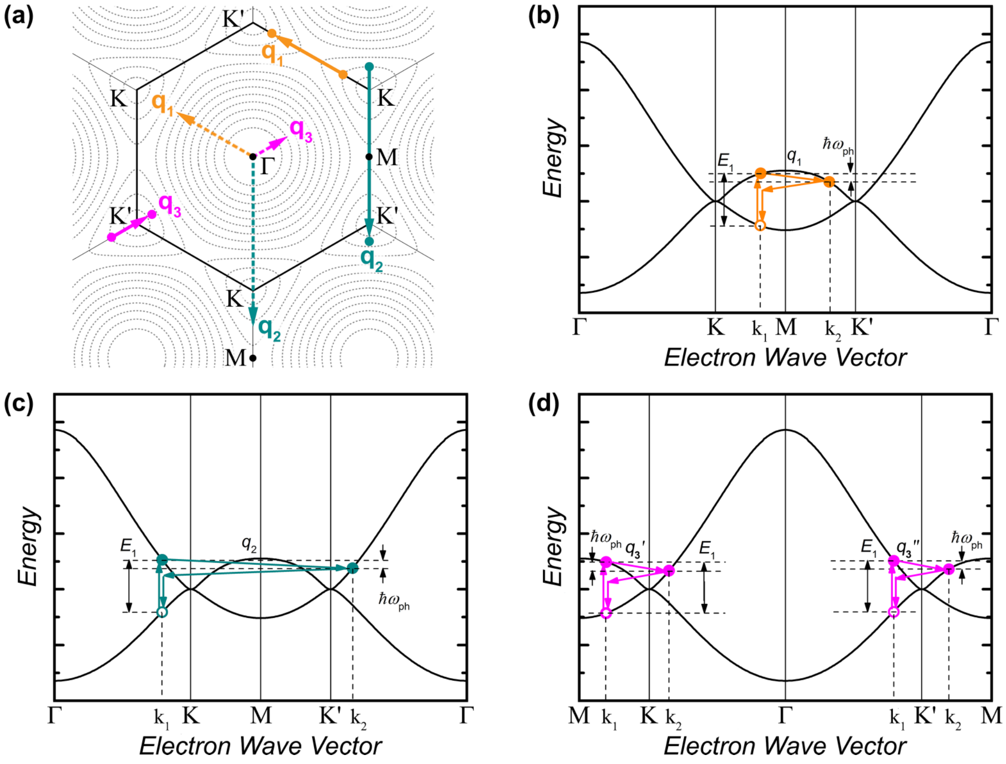

FIG. 10. (Color online) Double-resonant Raman-scattering processes. (a) Brillouin zone of graphite showing electron energy contours (black dashed lines). Intervalley scattering processes $q_1$ (orange solid arrow) involve two phonons belonging to the iTO branch along the Γ–K direction. Intervalley scattering processes $q_2$ (teal solid arrow) involve two phonons belonging to the iTO branch along the K-M direction as $q_2$ can be translated with a reciprocal lattice translational vector to lie along K–M. Intravalley scattering processes $q_3$ (magenta solid arrow) involve two phonons belonging to the LO branch. The corresponding dashed arrows have the same directions and lengths as the solid arrows and are used to denote the phonon wave vectors originating from the Brillouin-zone center (Γ point). (b)–(d) Energy wave-vector diagrams indicating corresponding scattering processes in (a). Photon energy resulting in the creation of an electron-hole pair $E_1$, corresponding electron wave vector $k_1$, energy loss by phonon generation $\hbar\omega_{\mathrm{ph}}$, and corresponding electron wave vector $k_2$, are indicated on each graph and are exaggerated for clarity.

phonons and two identical LO phonons, respectively, hence we have defined the frequency of each created phonon as

$$\omega_{\mathrm{ph,iTO}} = \frac{\omega_{\mathrm{ph,2iTO}}}{2} \text{ and } \omega_{\mathrm{ph,LO}} = \frac{\omega_{\mathrm{ph,2LO}}}{2}. \qquad \text{(C2)}$$

In the above equations, $\omega_{\mathrm{ph,2iTO}}$ and $\omega_{\mathrm{ph,2LO}}$ are the frequencies of the second-order Raman modes 2iTO and 2LO. For double-resonance scattering involving muliple polarizations, e.g., one iTO and one LA phonon, we cannot directly use the measured phonon frequency in Eq. (C1) because the two nonidentical phonons have different frequencies. Thus to determine $E_2$ we use the phonon energy for the LO polarization determined from $\frac{1}{2}\omega_{\mathrm{ph,2LO}}$ since the excited electron has been observed to first scatter with an optical phonon then relax by scattering with an acoustic phonon [54]. Since the first scattering process is identical for iTO + LA and 2iTO, the phonon wave vector involved is the same for both processes and justifies this method. The electronic band structure for graphite (Fig. 9) is then used to determine the value of the scattered electron's wave vector at $E_2(k_2)$.

The inelastic processes involved in double-resonance scattering can occur within the same electronic band or between two different electronic bands. However, resonance is canceled due to destructive interference effects for scattering across the Γ point between two nonparallel electronic bands [50]. Thus, the two possible double-resonance scattering processes are as follows: (i) intervalley scattering across the the Γ point between nonidentical K points, namely, the K and K′ points and (ii) intravalley scattering across the K or K′ point or between identical K points, which will be discussed in the following sections.

#### *a. Intervalley scattering*

Intervalley scattering between K and K′ electrons creates a phonon with a wave vector of $q_1$ or $q_2$ depending on whether the electron is scattered along slow or fast transport directions. In order to conserve momentum, the magnitude of the phonon wave vector involved in the scattering process is determined from the difference between the excited and the scattered electron wave vectors $k_1$ and $k_2$, respectively, which connects a real state at $E_1(k_1)$ located around the K point to another real state $E_2(k_2)$ located around the K′ point [Figs. 10(a)–10(c)]. The phonon wave vectors are then determined as

$$q = k_{\Gamma-\mathrm{K}} \pm (|k_1| + |k_2|), \qquad \text{(C3)}$$

where $k_{\Gamma-\mathrm{K}}$ is the magnitude of the zone-boundary wave vector at K, $k_1$ is determined from the laser exitation energy and electron band structure, and $k_2$ is determined as per Eq. (C1). The two values of $q$ for intervalley scattering arise from the anisotropic electron dispersion around K, which consists of a fast transport direction along Γ-M and a slow transport direction along K-M. Based on the Raman $D$ mode's cross-sectional integration, the lower intensity peak of the $D$ mode occurs for the scattering between two locations along the slow transport direction, whereas the higher intensity peak of the $D$ mode occurs for the scattering between two locations along the fast transport direction [50,55]. Considering that the Raman $2D$ mode is the second-order overtone of the $D$ mode, we assign the lower intensity $2D_1$ mode to electron scattering between two slow transport locations denoted as $q_1$ in Figs. 10(a) and 10(b), whereas the higher intensity $2D_2$ mode is assigned to electrons scattered between two fast transport locations denoted as $q_2$ in Figs. 10(a) and 10(c). This results in $q_1$ lying along the Γ-K direction and $q_2$ lying along the K-M direction as shown in Fig. 10(a).

An additional intervalley scattering process involves one iTO and one LA phonon. The excited electron first scatters with an iTO phonon, then is relaxed to the virtual electronic state in a process involving an LA phonon. For this reason, the phonon wave vector for the iTO + LA polarization is the same as for the 2iTO polarization. The iTO + LA frequency only satisfies the experimentally observed frequencies along Γ–K, and so we only plot this process along the Γ–K direction similar to Refs. [33,34].

#### *b. Intravalley scattering*

The phonon created during the intravalley double-resonance scattering process across K (or across K′) has a wave vector $q_3$ around the Γ point [Figs. 10(a) and 10(d)]. Two possible scattering processes can originate from both sides of the K point and create phonons with wave vectors $q_3'$ and $q_3''$ as shown in Fig. 10(d). Since $\hbar\omega_{\mathrm{ph}}$ is much less than $E_1$, the phonon energy is usually neglected to yield $q_3 \approx 2k_1$, where $k_1$ is calculated from the electronic band structure without considering phonon energy loss $\hbar\omega_{\mathrm{ph}}$ [50]. We do not make this assumption here. The difference in phonon wave vectors $q_3'$ and $q_3''$ arising from the two distinct intravalley scattering processes is small compared with the difference of the two intervalley scatterings discussed in Appendix C 2 a, and so we define the intravalley phonon wave vector as the average of $q_3'$ and $q_3''$ as [50]

$$q_3' \text{ or } q_3'' = |k_1 + k_2|, \qquad \text{(C4a)}$$

$$q_3 = \frac{q_3' + q_3''}{2}. \qquad \text{(C4b)}$$

### 3. Comparison with *ab initio* phonon dispersion

With the excitation energy-phonon wave-vector relationships defined above, we can now estimate the uncertainty. As we are using the *ab initio* electron band structure and hence have not assumed a linear or isotropic $E(k)$ relationship around K, the major source of uncertainty is in determining $E_2(k_2)$. In the case that the phonon energy $\hbar\omega_{\mathrm{ph}}$ is neglected in Eq. (C1), we calculated that the scattered electron energy $E_2$ is overestimated by 6.6%–10.1% for $E_1 = 2.54 - 1.96$ eV for all Raman active modes and all UG samples. The phonon wave vector then has uncertainties arising from the uncertainty in $k_2$ as per Eq. (C3), which is on the order of −4.2% to 1.9%. In order to avoid these uncertainties, we have accounted for inelastic energy losses in our calculations, and thus we do not expect uncertainties in our phonon frequency-wave-vector determination to be greater than this range.

We compare the first-order Raman $G$ mode (LO) and the second-order Raman modes (2LO, 2iTO, and iTO + LA) with the *ab initio* phonon-dispersion calculation described in the main text. The experimental phonon dispersion matches the *ab initio* phonon dispersion well for the LO, 2LO, and iTO + LA polarizations. The measured 2iTO phonon frequency along Γ–K is slightly lower than the *ab initio* frequency. This small deviation is likely due to the approximations involved in computational modeling of the *ab initio* phonon-dispersion calculation.

## APPENDIX D: THERMAL CONDUCTIVITY MODELING WITH SIGNIFICANT CONTRIBUTION FROM THE oTA POLARIZATION

In addition to the calculation presented in the main text where the thermal conductivity contribution from the oTA polarization is assumed to be negligible, here we discuss the other limiting case where the relative contribution from the oTA polarization with respect to the iTA and LA polarizations is as large as that reported in Ref. [15] for five-layer graphene by adjusting the Grüneisen parameters for each polarization. In this case, we have used a boundary scattering mean-free path $l_b = 1.7\,\mu$m to fit the low-temperature experimental thermal conductivity of all the ultrathin graphite samples $\kappa_{\mathrm{UG}}$. The Grüneisen parameters of $\gamma_{\mathrm{LA}} = g_{\mathrm{LO'}} = 0.380T^{0.471}$, $\gamma_{\mathrm{iTA}} = \gamma_{\mathrm{iTO'}} = 0.155T^{0.471}$, and $\gamma_{\mathrm{oTA}} = \gamma_{\mathrm{oTO'}} = -0.044T^{0.471}$ were used to match the calculation results with the high-temperature thermal conductivity values for all samples. As shown in Fig. 11 and similar to the case presented in the main text for negligible contribution from oTA and oTO′ polarizations, although the calculated $\kappa_{\mathrm{UG}}$ values based on $B_i = \pi/4$ for the in-plane polarized modes and $B_o = \pi/2$ for the oTA modes fit well over the entire temperature range for the low-impurity-concentration regimes, this $B$ value considerably overpredicts the strength of isotope scattering in the 50% $^{13}$C sample compared to the experimental results. The isotope-scattering strength needs to be reduced by a factor of 12.5 in order to match the calculation result to the measured $\kappa_{\mathrm{UG}}$ of the 50% $^{13}$C sample. Thus we conclude that in this limit of large contribution of out-of-plane polarizations to the thermal conductivity, we need an even smaller value of $B$ to match the high-impurity-concentration regime, 12.5 times smaller than the isolated impurity value.

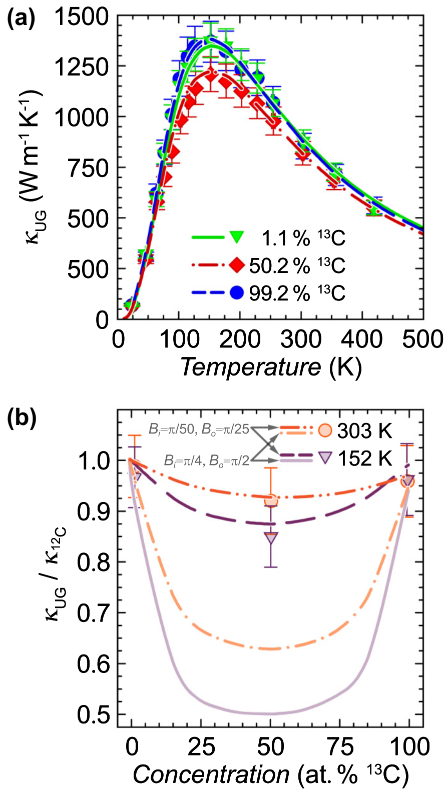

FIG. 11. (Color online) (a) Solid thermal conductivity of the ultrathin graphite ($\kappa_{\mathrm{UG}}$) versus temperature for $^{13}$C concentration of 1.1% (green down triangles), 50.2% (red diamonds), and 99.2% (blue circles). The lines are the calculated thermal conductivity based on the fitting parameters discussed in Appendix D for different $^{13}$C concentrations. (b) Calculated solid thermal conductivity normalized by the theoretical value for isotopically pure $^{12}$C graphite ($\kappa_{\mathrm{UG}}/\kappa_{^{12}\mathrm{C}}$) as a function of $^{13}$C isotopic concentration at temperatures of 152 K (purple down triangles) and 303 K (orange circles). In one calculation, the isotope-scattering coefficient $B$ is taken to be $B_i = \pi/4$ for the in-plane mode and $B_o = \pi/2$ for the out-of-plane modes. In another calculation, the two $B$ coefficients are reduced to $B_i = \pi/50$ for the in-plane mode and $B_o = \pi/25$.

---

[1] L. Lindsay, D. A. Broido, and T. L. Reinecke, Phonon-isotope scattering and thermal conductivity in materials with a large isotope effect: A first-principles study, Phys. Rev. B **88**, 144306 (2013).

[2] D. A. Broido, L. Lindsay, and T. L. Reinecke, *Ab initio* study of the unusual thermal transport properties of boron arsenide and related materials, Phys. Rev. B **88**, 214303 (2013).

[3] K. Belay, Z. Etzel, D. G. Onn, and T. R. Anthony, The thermal conductivity of polycrystalline diamond films: Effects of isotope content, J. Appl. Phys. **79**, 8336 (1996).

[4] M. Asen-Palmer, K. Bartkowski, E. Gmelin, M. Cardona, A. P. Zhernov, A. V. Inyushkin, A. Taldenkov, V. I. Ozhogin, K. M. Itoh, and E. E. Haller, Thermal conductivity of germanium crystals with different isotopic compositions, Phys. Rev. B **56**, 9431 (1997).

[5] D. T. Morelli, J. P. Heremans, and G. A. Slack, Estimation of the isotope effect on the lattice thermal conductivity of group IV and group III-V semiconductors, Phys. Rev. B **66**, 195304 (2002).

[6] J. H. Seol, I. Jo, A. L. Moore, L. Lindsay, Z. H. Aitken, M. T. Pettes, X. Li, Z. Yao, R. Huang, D. Broido, N. Mingo, R. S. Ruoff, and L. Shi, Two-dimensional phonon transport in supported graphene, Science **328**, 213 (2010).

[7] L. Lindsay and D. A. Broido, Enhanced thermal conductivity and isotope effect in single-layer hexagonal boron nitride, Phys. Rev. B **84**, 155421 (2011).

[8] I. Jo, M. T. Pettes, J. Kim, K. Watanabe, T. Taniguchi, Z. Yao, and L. Shi, Thermal conductivity and phonon transport in suspended few-layer hexagonal boron nitride, Nano Lett. **13**, 550 (2013).

[9] A. W. Smith, Low-temperature thermal conductivity of a Canadian natural graphite, Phys. Rev. **95**, 1095 (1954).

[10] J. C. Bowman, J. A. Krumhansl, and J. T. Meers, X-ray and low-temperature thermal conductivity study of defects in graphite, in *Industrial Carbon and Graphite* (Society of Chemical Industry, London, 1958), pp. 52–59.

[11] E. K. Sichel, R. E. Miller, M. S. Abrahams, and C. J. Buiocchi, Heat capacity and thermal conductivity of hexagonal pyrolytic boron nitride, Phys. Rev. B **13**, 4607 (1976).

[12] P. G. Klemens, The scattering of low-frequency lattice waves by static imperfections, Proc. Phys. Soc., London Sect. A **68**, 1113 (1955).

[13] S. Tamura, Isotope scattering of dispersive phonons in Ge, Phys. Rev. B **27**, 858 (1983).

[14] N. Mingo, K. Esfarjani, D. A. Broido, and D. A. Stewart, Cluster scattering effects on phonon conduction in graphene, Phys. Rev. B **81**, 045408 (2010).

[15] L. Lindsay, D. A. Broido, and N. Mingo, Flexural phonons and thermal transport in multilayer graphene and graphite, Phys. Rev. B **83**, 235428 (2011).

[16] I. Savić, N. Mingo, and D. A. Stewart, Phonon transport in isotope-disordered carbon and boron-nitride nanotubes: Is localization observable?, Phys. Rev. Lett. **101**, 165502 (2008).

[17] H. Sevinçli, W. Li, N. Mingo, G. Cuniberti, and S. Roche, Effects of domains in phonon conduction through hybrid boron nitride and graphene sheets, Phys. Rev. B **84**, 205444 (2011).

[18] H. C. Hottel, A. F. Sarofim, I. A. Vasalos, and W. H. Dalzell, Multiple scatter: Comparison of theory with experiment, J. Heat Transfer **92**, 285 (1970).

[19] H. C. Hottel, A. F. Sarofim, W. H. Dalzell, and I. A. Vasalos, Optical properties of coatings. Effect of pigment concentration, AIAA J. **9**, 1895 (1971).

[20] C. L. Tien and B. L. Drolen, Thermal radiation in particulate media with dependent and independent scattering, in *Annual Review of Numerical Fluid Mechanics and Heat Transfer*, edited by T. C. Chawla (Hemisphere, Washington, DC, 1987).

[21] C. W. Chang, A. M. Fennimore, A. Afanasiev, D. Okawa, T. Ikuno, H. Garcia, D. Li, A. Majumdar, and A. Zettl, Isotope effect on the thermal conductivity of boron nitride nanotubes, Phys. Rev. Lett. **97**, 085901 (2006).

[22] S. Chen, Q. Wu, C. Mishra, J. Kang, H. Zhang, K. Cho, W. Cai, A. A. Balandin, and R. S. Ruoff, Thermal conductivity of isotopically modified graphene, Nature Mater. **11**, 203 (2012).

[23] M. N. Luckyanova, J. Garg, K. Esfarjani, A. Jandl, M. T. Bulsara, A. J. Schmidt, A. J. Minnich, S. Chen, M. S. Dresselhaus, Z. Ren, E. A. Fitzgerald, and G. Chen, Coherent phonon heat conduction in superlattices, Science **338**, 936 (2012).

[24] J. Ravichandran, A. K. Yadav, R. Cheaito, P. B. Rossen, A. Soukiassian, S. J. Suresha, J. C. Duda, B. M. Foley, C.-H. Lee, Y. Zhu, A. W. Lichtenberger, J. E. Moore, D. A. Muller, D. G. Schlom, P. E. Hopkins, A. Majumdar, R. Ramesh, and M. A. Zurbuchen, Crossover from incoherent to coherent phonon scattering in epitaxial oxide superlattices, Nature Mater. **13**, 168 (2014).

[25] M. T. Pettes, H. Ji, R. S. Ruoff, and L. Shi, Thermal transport in three-dimensional foam architectures of few-layer graphene and ultrathin graphite, Nano Lett. **12**, 2959 (2012).

[26] Z. P. Chen, W. C. Ren, L. B. Gao, B. L. Liu, S. F. Pei, and H. M. Cheng, Three-dimensional flexible and conductive interconnected graphene networks grown by chemical vapour deposition, Nature Mater. **10**, 424 (2011).

[27] R. Lemlich, A theory for the limiting conductivity of polyhedral foam at low density, J. Colloid Interface Sci. **64**, 107 (1978).

[28] L. Shi, D. Y. Li, C. H. Yu, W. Y. Jang, D. Kim, Z. Yao, P. Kim, and A. Majumdar, Measuring thermal and thermoelectric properties of one-dimensional nanostructures using a microfabricated device, J. Heat Transfer **125**, 881 (2003).

[29] T. L. Bergman, A. S. Lavine, F. P. Incropera, and D. P. DeWitt, Chapter 3: One-dimensional, steady-state conduction, *Fundamentals of Heat and Mass Transfer* (Wiley, New York, 2011).

[30] M. A. Schuetz and L. R. Glicksman, A basic study of heat transfer through foam insulation, J. Cell. Plast. **20**, 114 (1984).

[31] J. H. Parker, D. W. Feldman, and M. Ashkin, Raman scattering by silicon and germanium, Phys. Rev. **155**, 712 (1967).

[32] T. R. Hart, R. L. Aggarwal, and B. Lax, Temperature dependence of Raman scattering in silicon, Phys. Rev. B **1**, 638 (1970).

[33] R. Saito, A. Jorio, A. G. Souza Filho, G. Dresselhaus, M. S. Dresselhaus, and M. A. Pimenta, Probing phonon dispersion relations of graphite by double resonance Raman scattering, Phys. Rev. Lett. **88**, 027401 (2001).

[34] C. Thomsen and S. Reich, Double resonant Raman scattering in graphite, Phys. Rev. Lett. **85**, 5214 (2000).

[35] S. Reich and C. Thomsen, Raman spectroscopy of graphite, Philos. Trans. R. Soc. London, Ser. A **362**, 2271 (2004).

[36] B. Abeles, Lattice thermal conductivity of disordered semiconductor alloys at high temperatures, Phys. Rev. **131**, 1906 (1963).

[37] P. Giannozzi *et al.*, QUANTUM ESPRESSO: A modular and open-source software project for quantum simulations of materials, J. Phys.: Condens. Matter **21**, 395502 (2009).

[38] N. Mounet and N. Marzari, First-principles determination of the structural, vibrational and thermodynamic properties of diamond, graphite, and derivatives, Phys. Rev. B **71**, 205214 (2005).

[39] X. S. Li, W. W. Cai, L. Colombo, and R. S. Ruoff, Evolution of graphene growth on Ni and Cu by carbon isotope labeling, Nano Lett. **9**, 4268 (2009).

[40] P. B. Allen and J. L. Feldman, Thermal conductivity of disordered harmonic solids, Phys. Rev. B **48**, 12581 (1993).

[41] G. Chen, Chapter 6: Particle description of transport processes: Classical laws, *Nanoscale Energy Transport and Conversion: A Parallel Treatment of Electrons, Molecules, Phonons, and Photons* (Oxford University Press, New York, 2005).

[42] M. M. Sadeghi, I. Jo, and L. Shi, Phonon-interface scattering in multi-layered graphene on an amorphous support, Proc. Natl. Acad. Sci. U.S.A. **110**, 16321 (2013).

[43] J. Callaway, Model for lattice thermal conductivity at low temperatures, Phys. Rev. **113**, 1046 (1959).

[44] P. G. Klemens and D. F. Pedraza, Thermal conductivity of graphite in the basal plane, Carbon **32**, 735 (1994).

[45] D. L. Nika, E. P. Pokatilov, A. S. Askerov, and A. A. Balandin, Phonon thermal conduction in graphene: Role of umklapp and edge roughness scattering, Phys. Rev. B **79**, 155413 (2009).

[46] P. G. Klemens, Thermal conductivity and lattice vibrational modes, in *Solid State Physics*, edited by F. Seitz and D. Turnbull (Academic Press, New York, 1958), pp. 1–98.

[47] R. Berman, P. T. Nettley, F. W. Sheard, A. N. Spencer, R. W. H. Stevenson, and J. M. Ziman, The effect of point imperfections on lattice conduction in solids, Proc. R. Soc. London, Ser. A **253**, 403 (1959).
[48] R. Berman and J. C. F. Brock, The effect of isotopes on lattice heat conduction. I. Lithium fluoride, Proc. R. Soc. London, Ser. A **289**, 46 (1965).
[49] A. M. Rappe, K. M. Rabe, E. Kaxiras, and J. D. Joannopoulos, Optimized pseudopotentials, Phys. Rev. B **41**, 1227(R)(1990).
[50] J. Maultzsch, S. Reich, and C. Thomsen, Double-resonant Raman scattering in graphite: Interference effects, selection rules, and phonon dispersion, Phys. Rev. B **70**, 155403 (2004).
[51] A. C. Ferrari, J. C. Meyer, V. Scardaci, C. Casiraghi, M. Lazzeri, F. Mauri, S. Piscanec, D. Jiang, K. S. Novoselov, S. Roth, and A. K. Geim, Raman spectrum of graphene and graphene layers, Phys. Rev. Lett. **97**, 187401 (2006).
[52] A. C. Ferrari, Raman spectroscopy of graphene and graphite: Disorder, electron–phonon coupling, doping and nonadiabatic effects, Solid State Commun. **143**, 47 (2007).
[53] L. M. Malard, M. A. Pimenta, G. Dresselhaus, and M. S. Dresselhaus, Raman spectroscopy in graphene, Phys. Rep. **473**, 51 (2009).
[54] V. V. Deshpande, S. Hsieh, A. W. Bushmaker, M. Bockrath, and S. B. Cronin, Spatially resolved temperature measurements of electrically heated carbon nanotubes, Phys. Rev. Lett. **102**, 105501 (2009).
[55] J. Kürti, V. Zólyomi, A. Grüneis, and H. Kuzmany, Double resonant Raman phenomena enhanced by van Hove singularities in single-wall carbon nanotubes, Phys. Rev. B **65**, 165433 (2002).
[56] J. Y. Howe, L. E. Jones, H. Ow, and C. J. Rawn, Improved crystallographic data for graphite, Powder Diffr. **18**, 150 (2003).
[57] C. Klein, Pyrolytic graphites: Their description as semimetallic molecular solids, J. Appl. Phys. **33**, 3338 (1962).
[58] D. E. Soule, Magnetic field dependence of the Hall effect and magnetoresistance in graphite single crystals, Phys. Rev. **112**, 698 (1958).